Nanoscale
Advances

ROYAL SOCIETY OF CHEMISTRY

PAPER

View Article Online
View Journal | View Issue

Cite this: *Nanoscale Adv.*, 2022, **4**, 4344

High-efficiency modulation of broadband polarization conversion with a reconfigurable chiral metasurface

Zeyong Wei,[ab] Yunlong Zhao,[ab] Yujing Zhang,[c] Weiqi Cai,[c] Yuancheng Fan,*[c]
Zhanshan Wang[ab] and Xinbin Cheng*[ab]

We demonstrate an electrically biased reconfigurable chiral metasurface for controlling the polarization conversion and asymmetric transmission in a broadband manner. The reconfigurable metasurface is constructed with coupled three-layer complementary split-ring resonator (CSRR) arrays and is loaded with tunable electronic components to achieve dynamic control of reconfigurable chiral coupling in the CSRRs by simply tuning the external voltage on the structure. It is found that the polarization conversion in the metasurface can be effectively and continuously tuned in both experiments and simulations in a broadband frequency range. Meanwhile, the reconfigurable metasurface shows an asymmetric transmission (AT) effect in a broadband range for a polarized wave. The proposed reconfigurable chiral metasurface based on the active tuning of connection in the meta-structure with few functional layers is confirmed as an effective strategy for multi-functional polarization manipulation. The reported broadband properties of the chiral metasurface are promising for polarization manipulation in optical bands and applications in wireless communication.

Received 15th June 2022
Accepted 30th August 2022

DOI: 10.1039/d2na00382a

rsc.li/nanoscale-advances

Introduction

Controlling of the polarization state of light is of fundamental importance in optics due to the vectorial nature of light waves.[1,2] Traditionally, polarization control is always realized by exploiting the propagation or total internal reflection of bulk materials or structures such as gratings, birefringent materials and liquid crystals.[3–6] The huge volume compared to the wavelength of light and the low efficiency of conventional polarization devices severely limit their applications, especially in the engaging nanophotonics. Optical/electromagnetic metasurfaces are artificial thin-layered structures composed of subwavelength resonant meta-cells, and with them, the transmission, polarization, phase, and complex wavefront of electromagnetic waves can be freely tuned by properly designing the unit structures and their spatial arrangements.[7–16]

The metasurface has been exploited for high-performance anisotropic and even chiral optics for its arbitrarily designed microstructure with superiority in achieving enhanced anisotropic scatterings of the vectorial components of electromagnetic waves.[17–30] It has been demonstrated as an excellent platform for high efficiency polarization control devices with ultrathin or subwavelength dimensions overcoming the conventional devices with macroscopic geometries. Meanwhile, the asymmetric transmission (AT) effect assisted by polarization conversion in a metasurface becomes an important subject for novel applications in non-reciprocal optical devices.[31–38] The metasurface based polarization manipulation has been applied in advanced wave devices.[39] However, the wave function of a metasurface is always fixed and limited in a narrow frequency range once the metasurface is fabricated due to which its strong dispersion control on the EM wave is achieved based on the resonant mechanisms of meta-atoms. The broadband and multifunctional features of metasurfaces are highly desirable for overcoming the barriers obstructing metasurfaces from practical applications in *e.g.* high-performance polarization manipulating devices.

The operation band of a metasurface can be widened effectively considering the interlayer coupling effect of the local resonant modes;[40] the laminated structure of the anisotropic open resonant ring has been employed to realize the broadband polarization conversion and asymmetric transmission.[41] The AT effect and polarization conversion of electromagnetic waves on the metasurface structures have been studied in the range of microwaves,[42–47] terahertzs[48–51] and optical band.[52–56] The design of these structures can be used for polarizers and have practical applications in imaging, communication and sensing.[7]

---

[a] School of Physics Science and Engineering, MOE Key Laboratory of Advanced Micro-Structured Materials, Institute of Precision Optical Engineering, Tongji University, Shanghai 200092, China. E-mail: chengxb@tongji.edu.cn

[b] Shanghai Frontiers Science Research Base of Digital Optics, Tongji University, Shanghai 200092, China

[c] Key Laboratory of Light Field Manipulation and Information Acquisition, Ministry of Industry and Information Technology, School of Physical Science and Technology, Northwestern Polytechnical University, Xi'an 710129, China. E-mail: phyfan@nwpu.edu.cn

Although these designed metasurface structures can achieve high efficiency and broadband AT effects, once these metasurface structures are designed, their function and performance are fixed and lack effective tunability, which limits their practical applications. Recently, the emergence of metasurface structures has greatly contributed to the tunability of electromagnetic waves. Dynamically tunable metamaterials can be obtained by introducing graphene, phase change materials (*e.g.*, vanadium dioxide and GST) and a nonlinear mechanism[57–73] for active control of light *e.g.* its polarization states. However, the current reconfigurable chiral metasurfaces always operate in a narrow frequency range and discrete polarization states,[74–78] and broadband continuous modulation of polarization is seldom reported.

In this paper, we demonstrate a reconfigurable chiral metasurface made of three-layer complementary split ring resonator (CSRR) arrays. The CSRRs on the middle layer are 45° -rotated with respect to the bottom layer, and a top CSRR array is incorporated with PIN diodes for simply controlling the direction of CSRRs with electric biasing. The vertically arranged few-layer structure provides the opportunity to effectively control the mutual coupling and chiroptical effect operating in a broadband manner.[40] Furthermore, the top layer with tunable electric connection between the four arms provides a reconfigurable metasurface platform for controlling the chiral coupling between the near-neighboring CSRRs for polarization manipulation and the AT effect.[25,79] Our proof of principle with a microwave reconfigurable chiral metasurface verified that the polarization conversion and AT effect can be switched in a wide frequency band by electrically tuning the orientation of CSRRs on the top layer. More interestingly, it shows that the polarization conversion is controlled continuously by varying the external excitation voltage. The reconfigurable chiral metasurfaces based on the active tuning of connection in meta-atoms can be extended to other metasurfaces with multiple functions and potential applications in antennas and wireless communications, such as polarization multiplexing-based 5G communications.

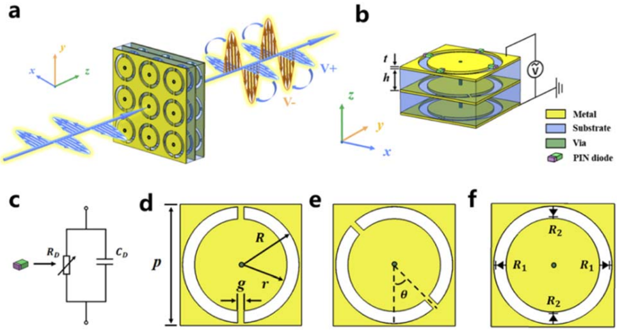

Fig. 1 (a) Schematic illustration of the chiral metasurface with electrically tunable polarization conversion. (b) Perspective view of a unit cell of the metasurface. (c) Diode equivalent circuit model of the employed PIN diode (the electric circuit model parameter R_D of the PIN diode is controlled by varying the external excitation voltage). The unit structure on the bottom layer (d), the middle layer (e), and the top layer (f) (R_1 is the equivalent resistance of the two diodes in the x-direction and R_2 is the resistance parameter of the two diodes in the y-direction).

Results and discussion

The micro-structure of the reconfigurable chiral metasurface and its operation principle of the electrically controlled broadband polarization conversion are schematically illustrated in Fig. 1. The chiral metasurface is composed of three-functional metallic layers, and the three layers with a thickness of $t = 0.035$ mm are separated by dielectric substrates with a relative dielectric constant of 2.65 and a thickness of $h = 1.55$ mm. The patterned metallic arrays can be seen from the perspective view of a unit cell of the metasurface (Fig. 1b) and detailed micro-structures on different layers (Fig. 1d–f). The functional layers are composed of complementary split/non-split ring resonator arrays with a period of $p = 10$ mm. The anisotropy split ring resonator array of the metasurface enables the polarization conversion and AT effect of electromagnetic waves. A complementary open splitting circle with 45°-rotated in the middle layer provides the opportunity to achieve chiral coupling in the metasurface which has been demonstrated to be of fundamental importance in realizing metasurfaces operating in a broadband manner.[24] To achieve dynamic manipulation of the polarization, we need to change the bias voltage of the PIN diodes loaded on the CSRRs. In practice, we use an array of metal vias to connect the circular patches of the top CSRR layer and the bottom CSRR layer, so the resistances of the PIN diodes can be controlled by applying the bias voltage on the first and third layer of the metal mesh grid, while the polarization state of the transmitted wave can be precisely controlled.

For realizing the active tunability of the broadband polarization control in the metasurface, we use an array of PIN diodes [MACOM MA4AGP907] loaded between the gap of CSRRs. The Aluminum Gallium Arsenide (AlGaAs) flip-chip PIN diodes (MA4AGP907) have a small junction capacitance of 0.025 pF, so the PIN diode can be simply modeled as a parallel RC circuit with a constant capacitance and a tunable resistance (Fig. 1c).[80] The variable resistance of the diodes changes from infinite to 4.2 Ω, while the bias voltage increases positively from 0 to +1.25 V. The diodes are divided into two pairs with opposite electric biasing for controlling the electric connection between the inside and outside of the annulus (Fig. 1b and f). Then the orientation of the CSRRs on the top layer can be reconfigured by precisely and continuously tuning biasing voltage on the metasurface. When a maximum forward voltage is applied, the incident x-polarized wave remains as x-polarized wave after passing through the metasurface, with a polarization rotation angle of 0° compared to the incident wave. However, if we reduce the applied voltage from the maximum forward voltage to negative voltage, the transmitted wave will be a y-polarized wave, and the polarization is rotated by 90° compared to the incident wave. The structure of the meta-unit (Fig. 1b) as well as the chiral coupling in the three CSRRs can be simply applying electric voltages. Then the polarization of the incident linearly polarized electromagnetic wave or light wave can be dynamically rotated from 0° to 90° in a broad functional band of the metasurface device.

For the polarization conversion properties of the proposed metasurface, we employed a finite difference time domain (FDTD) method based electromagnetic full wave solver for the numerical simulations in which the metallic resonant structures are set as PEC, and the electric circuit model parameters of the PIN diode are $R_D = 4.2\ \Omega$ and $C_D = 0.025$ pF. The inner and outer radii of the bottom layer, middle layer and top layer of the metal element structure are $R = 4.8$ mm and $r = 4.2$ mm. The rings in a unit are symmetrically segmented by two metallic strips with a width of $g = 0.2$ mm and $\theta = 45°$. Periodic boundary conditions are set along the x-axis and y-axis of the element structure, and the linearly polarized electromagnetic wave propagates along the z-axis positive direction. The geometrical shape of metal resonant elements in the metasurface lacks mirror symmetry, which results in strong electromagnetic wave cross coupling in the structure. The cross coupling and corresponding polarization transformation ensure the AT effect in the wide frequency band.

The cross-coupling and cross-polarization of electromagnetic waves cause the asymmetric propagation of electromagnetic waves in the metasurface, which is asymmetric to the opposite direction of propagation. Considering the plane electromagnetic wave incident to the metasurface structure in the positive direction (+z), the following equation can be obtained:[81]

$$E_i(r,t) = \begin{pmatrix} I_x \\ I_y \end{pmatrix} e^{i(kz-\omega t)} \tag{1}$$

in which ω is the angular frequency, k is the wave vector, I_x and I_y are the complex amplitudes of the electric field in the x and y directions, respectively, which describe the state of polarization. Therefore, the transmitted field can be expressed as:

$$E_t(r,t) = \begin{pmatrix} T_x \\ T_y \end{pmatrix} e^{i(kz-\omega t)} \tag{2}$$

The Jones matrix T is used to describe the relationship between the incident wave and transmitted wave and can be expressed as:

$$\begin{pmatrix} T_x \\ T_y \end{pmatrix} = \begin{bmatrix} t_{xx} & t_{xy} \\ t_{yx} & t_{yy} \end{bmatrix} \begin{pmatrix} I_x \\ I_y \end{pmatrix} = T^f_{\text{lin}} \begin{pmatrix} I_x \\ I_y \end{pmatrix} \tag{3}$$

in which the superscript-f and subscript-lin respectively refer to the forward (+z) direction propagation of plane electromagnetic waves and special linear bases with basis vectors parallel to the coordinate axes. According to the reciprocal theorem, the electromagnetic wave T matrix[82] propagating along the reverse ($-z$) direction can be obtained:

$$T^b_{\text{lim}} = \begin{bmatrix} t_{xx} & -t_{yx} \\ -t_{xy} & t_{yy} \end{bmatrix} \tag{4}$$

where the superscript-b represents the backward ($-z$) direction propagation of the plane electromagnetic wave. To calculate the polarization conversion performance of the metasurface, the polarization conversion rate (PCR) can be defined:

$$\text{PCR}_x = |t_{yx}|^2/(|t_{yx}|^2 + |t_{xx}|^2) \tag{5}$$

$$\text{PCR}_y = |t_{xy}|^2/(|t_{xy}|^2 + |t_{yy}|^2) \tag{6}$$

$$T_{ij} = |t_{ij}| \tag{7}$$

t_{ij} represents the transmission coefficient of the transmitted wave polarized in the i direction caused by the j-polarized incident wave ($i, j = x$ or y).

For opposite propagation directions, the difference of off-diagonal elements in the T-matrix is the main reason for the phenomenon of asymmetric transmission in the metasurface structure. The asymmetric transmission of an incident electromagnetic wave propagating in the opposite direction can be expressed by the intensity difference:

$$\Delta^x_{\text{lin}} = |t^f_{xx}|^2 + |t^f_{yx}|^2 - |t^b_{yx}|^2 - |t^b_{xx}|^2 = |t^f_{yx}|^2 - |t^f_{xy}|^2 \tag{8}$$

$$\Delta^y_{\text{lin}} = -\Delta^x_{\text{lin}} \tag{9}$$

For linearly polarized electromagnetic waves $t^{f(b)}_{xx} = t^{f(b)}_{yy}$ and $t^{f(b)}_{yx} \neq t^{f(b)}_{xy}$; this means that the intensity and phase of the polarization state are different in opposite propagation directions. The electromagnetic simulation of the proposed transmissive unit is carried out with help of the finite-difference time-domain (FDTD) software named Gallop by using periodic boundary conditions. Numerical calculations were carried out to study the polarization conversion and asymmetric transmission effect of the linearly polarized electromagnetic wave normal incident to the metasurface structure along the z-axis in two states of PIN diodes. Fig. 2a shows the transmission coefficient of the electromagnetic wave propagating forward along the z-axis when the diode is on in the x direction and disconnected in the y direction (state 1). At this point, the y-polarized wave can excite the resonant mode of the top structure and realize the transmission of the y-polarized electromagnetic wave. It can be clearly seen that in the broadband range of 8.3–11.2 GHz, the cross-polarization transmission coefficient T_{yx} of the x-polarized wave transformed into a y-polarized wave exceeds 0.8 and reaches the maximum of 0.96 at 9.8 GHz.

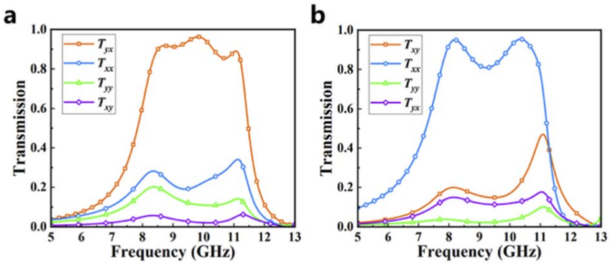

Fig. 2 Transmission coefficient of the linearly polarized wave under normal incidence along the z-axis with different sets of the two paired PIN diode: state 1 (a) and state 2 (b).

However, the transmission coefficient T_{xy} is very small in this frequency band range, and the difference between T_{yx} and T_{xy} leads to high polarization conversion. The transmission coefficient T_{xx} without polarization conversion in the whole frequency band is far less than the cross-polarization transmission coefficient T_{yx}, that is, there is almost no transmission of the same polarization electromagnetic wave in the whole frequency band range. Fig. 2b shows the results for the case the diode is disconnected in the x direction and turned on in the y direction (state 2); the transmission coefficient of the electromagnetic wave propagates forward along the z-axis. At the top of the structure in the x polarization mode, at the same time, due to the underlying structure being in the x polarization mode, bottom and top with the same polarization mode, linearly polarized electromagnetic wave incident to the metasurface structure, the x-polarized wave can excite the resonant mode at the bottom, and the outgoing wave is also an x-polarized wave through the near-field coupling of the local mode between layers. As can be seen from the figure, an x-polarized linearly wave is transmitted. The transmission coefficient T_{xx} reaches the maximum of 0.96 at 10.3 GHz and exceeds 0.8 at 7.8–10.8 GHz. And the transmission coefficient T_{yy} is very small in this band range. It can also be clearly seen that the transmission coefficient T_{yx} is very small, so there is no polarization conversion of the incident electromagnetic wave. In addition, state 3: the diode is disconnected in both the x and y directions and is presented in order to demonstrate the function of the metasurface.

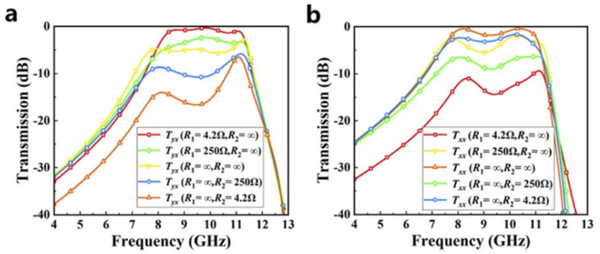

Fig. 3 Calculated transmission spectra for cross-polarization (a) T_{yx} and co-polarization (b) T_{xx} for the designed metasurface with different resistance parameters.

From the transmission spectra of the linearly polarized electromagnetic wave under different sets of biasing of the active diode, the highly efficient and broadband modulation on the polarization conversion of linearly polarized incidence can be realized by changing the setting of the resistance of the two paired diode. Intuitively, we expected to achieve continuously controlled polarization conversion in a broadband manner by precisely tuning the setup of resistance between state 1, state 3 and state 2. The continuous adjustment of the transmission coefficient and cross-polarization transmission coefficient by changing the resistance of the diodes in the two directions is confirmed through numerical simulations as shown in Fig. 3. When the resistance $R_1 = 4.2\ \Omega$ in the x direction and $R_2 = \infty$ in the y direction, the cross-polarization transmission coefficient T_{yx} is about 0.96, and the transmission coefficient T_{xx} is about 0.3, corresponding to state 1. T_{yx} decreases and T_{xx} increases when R_1 increases and R_2 remains constant. $T_{yx} = 0.58$ and $T_{xx} = 0.8$ when R_1 and R_2 are infinite, corresponding to state 3. Then, as R_1 remains constant, T_{yx} continues to decrease, and T_{xx} continues to increase as R_2 increases until state 2 is reached when $R_1 = \infty$ and $R_2 = 4.2\ \Omega$ and $T_{yx} = 0.2$ and $T_{xx} = 0.96$. Therefore, the polarization state can be dynamically and continuously changed by adjusting the parameters of the diode, so as to realize the polarization conversion of the x-polarized wave to a y-polarized wave when the linearly polarized electromagnetic wave is incident on the metasurface or only the linearly polarized electromagnetic wave passes through the metasurface.

To elucidate the physical mechanism of the broadband and tunable polarization transformation in the metasurface, we calculated the electric field distribution around the metasurface under different sets of resistances as shown in Fig. 4. It can be seen that the incident wave of x-polarization changes the degree of polarization rotation after passing through the super-surface with different voltages applied. We can conclude that the

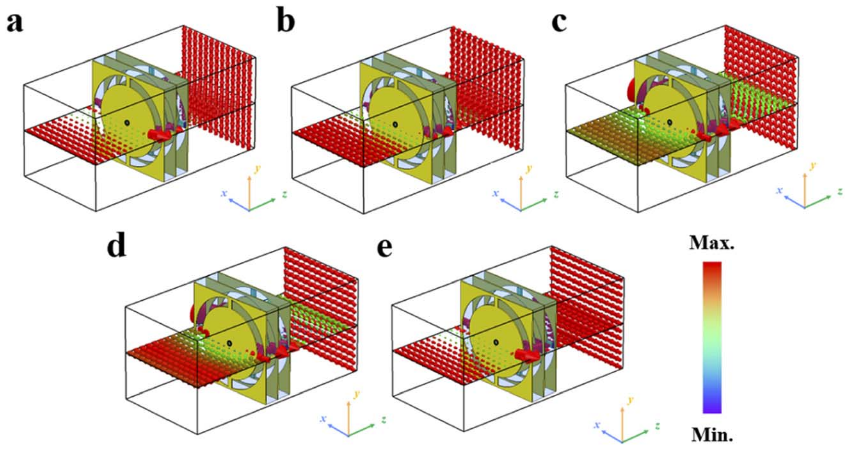

Fig. 4 Investigation on the electric field incident on and passing through the metasurface with different sets of resistance parameters corresponding to Fig. 3: (a) $R_1 = 4.2\ \Omega$; $R_2 = \infty$. (b) $R_1 = 250\ \Omega$; $R_2 = \infty$. (c) $R_1 = \infty$; $R_2 = \infty$. (d) $R_1 = \infty$; $R_2 = 250\ \Omega$. (e) $R_1 = \infty$; $R_2 = 4.2\ \Omega$.

polarization control is achieved by adjusting the coupling effect between the local resonance modes of each layer through the 45° angular deflection of the intermediate layer. Therefore, the characteristics of the electromagnetic wave can be dynamically regulated by controlling the conduction direction of the top diode. The polarization conversion and asymmetric transmission effect of electromagnetic waves can be realized when the diode is in state 1: x direction, and the diode is disconnected in the y direction. When the diode is disconnected in the x direction and turned on in the y direction in state 2, the electromagnetic wave does not have these characteristics.

In this work, to verify the metasurface performance experimentally, we used the printed circuit board (PCB) technique to fabricate a metasurface sample containing 144 (12×12) unit cells as shown in Fig. 5a. We measured the cross-polarization transfer coefficient and co-polarization transfer coefficient at −1.25 V to 0 V to +1.25 V bias; the variable resistance R_1 of the diode changes from $R_1 = 4.2\ \Omega$ to infinite, while the bias voltage decreases in reverse from −1.25 V to 0, and the variable resistance R_2 of the diode changes from infinite to $R_2 = 4.2\ \Omega$, while the bias voltage increases positively from 0 to +1.25 V (Fig. 5b is the metasurface under testing). The transmission spectra at five sets of bias voltages are experimentally studied, and the simulation results are given for the corresponding circuit model equivalent parameters. We compared the experimental and simulation results in Fig. 5c and d. It is clearly shown: (i) the incident x-polarized wave at state 1: −1.25 V bias voltage ($R_1 = 4.2\ \Omega$; $R_2 = \infty$) and state 2: +1.25 V bias voltage ($R_1 = \infty$; $R_2 = 4.2\ \Omega$) has a high cross-polarization transfer coefficient and co-polarization transfer coefficient over a wide frequency range; (ii) the ratio of the converted y-polarized wave can be dramatically and continuously modulated by tuning the biasing voltage on the metasurface sample.

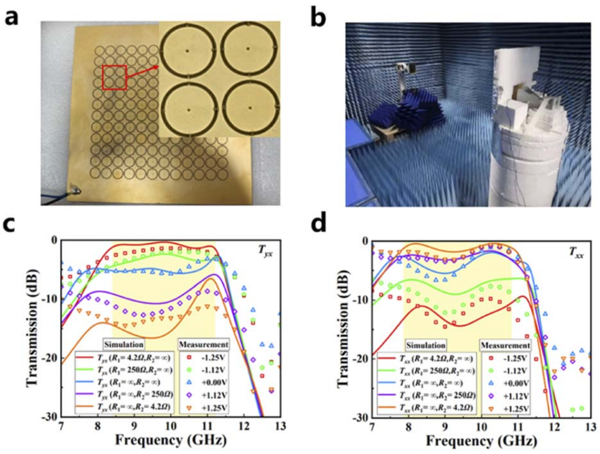

Fig. 5 (a) Photograph of the reconfigurable chiral metasurface. (b) Photograph of the experiment environment. Comparison of measured and experimental transmission spectra for cross-polarization (c) T_{yx} and co-polarization (d) T_{xx} for the fabricated metasurface sample in different states.

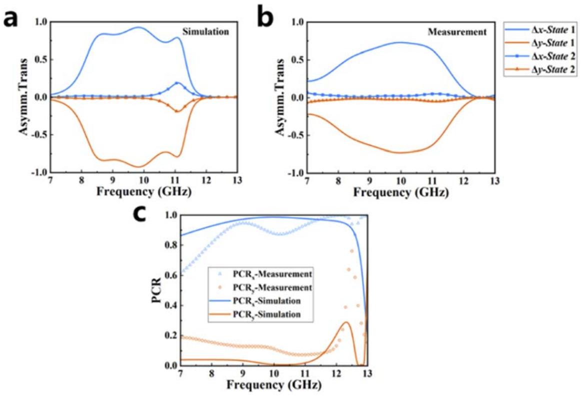

Fig. 6 Simulated (a) and measured (b) asymmetric transmission spectra and the (c) polarization conversion ratio for the chiral metasurface operating in different states.

We further studied the asymmetric transmission feature of the metasurface. The measured and simulated results of the asymmetric transmission spectra and polarization conversion efficiency of the diode in different states are presented in Fig. 6. The maximum value of Δx in simulation is 0.92 at 9.8 GHz (Fig. 6a), and the asymmetric transmission characteristic is displayed in the 8.4–11.2 GHz band in state 1. For state 2, the maximum value of Δx is 0.19 at 11.0 GHz, and no asymmetric transmission characteristic is displayed. Fig. 6b shows that the measured results for $\Delta x(y)$ in states 1 and 2 agreed well with the theoretical calculations. The polarization conversion rate (PCR) represents the conversion amount of one linearly polarized wave to another. According to formula (5) and (6), the PCR of the linearly polarized electromagnetic wave can be calculated. Fig. 6c shows the comparison of polarization conversion rates between the simulation and experiment. As for the simulated results, it can be seen that the PCR value of x-polarized wave exceeds 93% in the broadband 8.1 GHz to 11.6 GHz, and the PCR value of the y-polarized wave is less than 10% at the same operating frequency. Therefore, in this case, the electromagnetic wave realizes the polarization conversion of the x-polarized wave incident to the y-polarized wave. The experimentally measured results are consistent with the simulated results. The active metasurface with three specifically designed complementary structures is proved to be a good platform for achieving broadband tunable polarization conversion and asymmetric transmission.

Conclusions

In summary, we demonstrate a reconfigurable chiral metasurface with stacked CSRR arrays. The orientation of the CSRRs in different layers is properly designed and actively reconfigured considering the electric connection with PIN diodes. The chiroptical response or chiral coupling in the stacked CSRRs can be actively reconfigured by changing the biased voltage on the metasurface, and the cross-polarization transmission coefficient and transmission coefficient are continuously adjusted to realize the continuous polarization manipulation. The structures designed in this paper are practical in the microwave section and can be used as a frequency selector and converter among others to achieve multi-functional manipulation of electromagnetic waves through the reconfigurable metasurface structure in the broadband range. The proposed strategy for achieving multi-functional polarization control with a reconfigurable chiral metasurface can be extended to the optical regime considering the active research studies on actively modulated optical metasurfaces.

Author contributions

All authors commented on the manuscript.

Conflicts of interest

There are no conflicts to declare.

Acknowledgements

We are grateful for financial support from the National Natural Science Foundation of China (Grants No. 11874285, 12074314, 61621001, 61925504, 6201101335, 62020106009, 62061136008, and 62111530053).

Notes and references

1 H.-T. Chen, A. J. Taylor and N. Yu, *Rep. Prog. Phys.*, 2016, **79**, 076401.

2 A. Arbabi, Y. Horie, M. Bagheri and A. Faraon, *Nat. Nanotechnol.*, 2015, **10**, 937–943.

3 I. Yamada, K. Takano, M. Hangyo, M. Saito and W. Watanabe, *Opt. Lett.*, 2009, **34**, 274–276.

4 C.-Y. Chen, T.-R. Tsai, C.-L. Pan and R.-P. Pan, *Appl. Phys. Lett.*, 2003, **83**, 4497–4499.

5 M. Mutlu, A. E. Akosman and E. Ozbay, *Opt. Lett.*, 2012, **37**, 2094–2096.

6 K. Wiesauer and C. Jördens, *J. Infrared, Millimeter, Terahertz Waves*, 2013, **34**, 663–681.

7 N. Yu and F. Capasso, *Nat. Mater.*, 2014, **13**, 139–150.

8 A. V. Kildishev, A. Boltasseva and V. M. Shalaev, *Science*, 2013, **339**, 1232009.

9 N. Shitrit, I. Yulevich, E. Maguid, D. Ozeri, D. Veksler, V. Kleiner and E. Hasman, *Science*, 2013, **340**, 724–726.

10 B. Groever, W. T. Chen and F. Capasso, *Nano Lett.*, 2017, **17**, 4902–4907.

11 S. Sun, Q. He, S. Xiao, Q. Xu, X. Li and L. Zhou, *Nat. Mater.*, 2012, **11**, 426–431.

12 X. Chen, L. Huang, H. Mühlenbernd, G. Li, B. Bai, Q. Tan, G. Jin, C.-W. Qiu, S. Zhang and T. Zentgraf, *Nat. Commun.*, 2012, **3**, 1198.

13 S. Chen, W. Liu, Z. Li, H. Cheng and J. Tian, *Adv. Mater.*, 2020, **32**, 1805912.

14 W. Zhu, Y. Fan, R. Yang, G. Geng, Q. Fu, C. Gu, J. Li and F. Zhang, *Adv. Funct. Mater.*, 2022, **32**, 2200013.

15 Y. Zhang, H. Liu, H. Cheng, J. Tian and S. Chen, *Opto-Electron. Adv.*, 2020, **3**, 200002.

16 Y. Guo, X. Ma, M. Pu, X. Li, Z. Zhao and X. Luo, *Adv. Opt. Mater.*, 2018, **6**, 1800592.

17 S. Zhang, Y.-S. Park, J. Li, X. Lu, W. Zhang and X. Zhang, *Phys. Rev. Lett.*, 2009, **102**, 023901.

18 E. Plum, J. Zhou, J. Dong, V. A. Fedotov, T. Koschny, C. M. Soukoulis and N. I. Zheludev, *Phys. Rev. B: Condens. Matter Mater. Phys.*, 2009, **79**, 035407.

19 J. Hao, Y. Yuan, L. Ran, T. Jiang, J. A. Kong, C. T. Chan and L. Zhou, *Phys. Rev. Lett.*, 2007, **99**, 063908.

20 S. Zhang, J. Zhou, Y.-S. Park, J. Rho, R. Singh, S. Nam, A. K. Azad, H.-T. Chen, X. Yin, A. J. Taylor and X. Zhang, *Nat. Commun.*, 2012, **3**, 942.

21 J. Zhou, D. R. Chowdhury, R. Zhao, A. K. Azad, H.-T. Chen, C. M. Soukoulis, A. J. Taylor and J. F. O'Hara, *Phys. Rev. B: Condens. Matter Mater. Phys.*, 2012, **86**, 035448.

22 Y. Ye and S. He, *Appl. Phys. Lett.*, 2010, **96**, 203501.

23 Y. Zhao and A. Alù, *Phys. Rev. B: Condens. Matter Mater. Phys.*, 2011, **84**, 205428.

24 Z. Wei, Y. Cao, Y. Fan, X. Yu and H. Li, *Appl. Phys. Lett.*, 2011, **99**, 221907.

25 F. Neubrech, M. Hentschel and N. Liu, *Adv. Mater.*, 2020, **32**, 1905640.

26 B. Wang, W. Liu, M. Zhao, J. Wang, Y. Zhang, A. Chen, F. Guan, X. Liu, L. Shi and J. Zi, *Nat. Photonics*, 2020, **14**, 623–628.

27 Y. Chen, W. Du, Q. Zhang, O. Ávalos-Ovando, J. Wu, Q.-H. Xu, N. Liu, H. Okamoto, A. O. Govorov, Q. Xiong and C.-W. Qiu, *Nat. Rev. Phys.*, 2022, **4**, 113–124.

28 H. X. Xu, G. Hu, Y. Wang, C. Wang, M. Wang, S. Wang, Y. Huang, P. Genevet, W. Huang and C. W. Qiu, *Light: Sci. Appl.*, 2021, **10**, 75.

29 S. Liu, T. Jun Cui, A. Noor, Z. Tao, H. Chi Zhang, G. Dong Bai, Y. Yang and X. Yang Zhou, *Light: Sci. Appl.*, 2018, **7**, 18008.

30 M. Jia, Z. Wang, H. Li, X. Wang, W. Luo, S. Sun, Y. Zhang, Q. He and L. Zhou, *Light: Sci. Appl.*, 2019, **8**, 16.

31 V. A. Fedotov, P. L. Mladyonov, S. L. Prosvirnin, A. V. Rogacheva, Y. Chen and N. I. Zheludev, *Phys. Rev. Lett.*, 2006, **97**, 167401.

32 R. Singh, E. Plum, C. Menzel, C. Rockstuhl, A. K. Azad, R. A. Cheville, F. Lederer, W. Zhang and N. I. Zheludev, *Phys. Rev. B: Condens. Matter Mater. Phys.*, 2009, **80**, 153104.

33 C. Menzel, C. Helgert, C. Rockstuhl, E. B. Kley, A. Tünnermann, T. Pertsch and F. Lederer, *Phys. Rev. Lett.*, 2010, **104**, 253902.

34 C. Huang, Y. Feng, J. Zhao, Z. Wang and T. Jiang, *Phys. Rev. B: Condens. Matter Mater. Phys.*, 2012, **85**, 195131.

35 M. Kang, J. Chen, H.-X. Cui, Y. Li and H.-T. Wang, *Opt. Express*, 2011, **19**, 8347–8356.

36 Y. Cheng, Y. Nie, X. Wang and R. Gong, *Appl. Phys. A*, 2013, **111**, 209–215.

37 J. Shi, X. Liu, S. Yu, T. Lv, Z. Zhu, H. Feng Ma and T. Jun Cui, *Appl. Phys. Lett.*, 2013, **102**, 191905.

38 F. Zhang, M. Pu, X. Li, P. Gao, X. Ma, J. Luo, H. Yu and X. Luo, *Adv. Funct. Mater.*, 2017, **27**, 1704295.

39 Y. Huang, L. Yang, J. Li, Y. Wang and G. Wen, *Appl. Phys. Lett.*, 2016, **109**, 054101.

40 S. Chen, Y. Zhang, Z. Li, H. Cheng and J. Tian, *Adv. Opt. Mater.*, 2019, **7**, 1801477.

41 K. Y. Cheng, Z. Y. Wei, Y. C. Fan, X. M. Zhang, C. Wu and H. Q. Li, *Adv. Opt. Mater.*, 2019, **7**, 1900016.
42 S. H. A. Bokhari and H. M. Cheema, *J. Appl. Phys.*, 2020, **128**, 063102.
43 C. X. Huang, J. J. Zhang, L. Wu, C. Zhang, J. Yang, L. X. Yang, J. C. Ke, L. Bai, Q. Cheng and T. J. Cui, *Adv. Theory Simul.*, 2020, **3**, 2000109.
44 M. I. Khan, B. Hu, A. Amanat, N. Ullah, M. J. I. Khan and A. R. Khalid, *J. Phys. D: Appl. Phys.*, 2020, **53**, 305004.
45 F. Long, S. Yu, N. Kou, C. Zhang, Z. Ding and Z. Zhang, *J. Appl. Phys.*, 2020, **127**, 023104.
46 T. Ullah and A. Rashid, *Microw. Opt. Technol. Lett.*, 2020, **63**, 226–234.
47 L. Zhang, P. Zhou, H. Chen, H. Lu, H. Xie, L. Zhang, E. Li, J. Xie and L. Deng, *Sci. Rep.*, 2016, **6**, 33826.
48 J.-S. Li and F.-Q. Bai, *Opt. Mater. Express*, 2020, **10**, 1853–1861.
49 T. Lv, X. Chen, G. Dong, M. Liu, D. Liu, C. Ouyang, Z. Zhu, Y. Li, C. Guan, J. Han, W. Zhang, S. Zhang and J. Shi, *Nanophotonics*, 2020, **9**, 3235–3242.
50 W. Pan, Q. Chen, Y. Ma, X. Wang and X. Ren, *Opt. Commun.*, 2020, **459**, 124901.
51 Y. Rao, L. Pan, C. Ouyang, Q. Xu, L. Liu, Y. Li, J. Gu, Z. Tian, J. Han and W. Zhang, *Opt. Express*, 2020, **28**, 29855–29864.
52 Y. Ren, C. Jiang and B. Tang, *J. Opt. Soc. Am. B*, 2020, **37**, 3379–3385.
53 L. Zhou, Y. Wang, J. Zhou, J. Ding, M. Lu and T. Sang, *Appl. Opt.*, 2020, **59**, 6868–6872.
54 Y. Tian, Z. Chen, F.-F. Ren, Q. Du and Z. Li, *Front. Phys.*, 2021, **9**, 676840.
55 W. Xiong, C. W. Hsu, Y. Bromberg, J. E. Antonio-Lopez, R. Amezcua Correa and H. Cao, *Light: Sci. Appl.*, 2018, **7**, 54.
56 M. X. Ren, W. Wu, W. Cai, B. Pi, X. Z. Zhang and J. J. Xu, *Light: Sci. Appl.*, 2017, **6**, e16254.
57 S. Huang, C. Song, G. Zhang and H. Yan, *Nanophotonics*, 2017, **6**, 1191–1204.
58 Y. Y. Ji, F. Fan, X. H. Wang and S. J. Chang, *Opt. Express*, 2018, **26**, 12852–12862.
59 Y. Li, J. Lin, H. Guo, W. Sun, S. Xiao and L. Zhou, *Adv. Opt. Mater.*, 2020, **8**, 1901548.
60 J. Zhang, X. Wei, I. D. Rukhlenko, H.-T. Chen and W. Zhu, *ACS Photonics*, 2020, **7**, 265–271.
61 Y. Zhang, Y. Feng, B. Zhu, J. Zhao and T. Jiang, *Opt. Express*, 2015, **23**, 27230–27239.
62 A. V. Pogrebnyakov, J. A. Bossard, J. P. Turpin, J. D. Musgraves, H. J. Shin, C. Rivero-Baleine, N. Podraza, K. A. Richardson, D. H. Werner and T. S. Mayer, *Opt. Mater. Express*, 2018, **8**, 2264–2275.
63 Y. Qu, Q. Li, L. Cai, M. Pan, P. Ghosh, K. Du and M. Qiu, *Light: Sci. Appl.*, 2018, **7**, 26.
64 J. Tian, H. Luo, Y. Yang, F. Ding, Y. Qu, D. Zhao, M. Qiu and S. I. Bozhevolnyi, *Nat. Commun.*, 2019, **10**, 396.
65 J. Tian, H. Luo, Y. Yang, F. Ding, Y. Qu, D. Zhao, M. Qiu and S. I. Bozhevolnyi, *Nat. Commun.*, 2019, **10**, 396.
66 P. Pitchappa, A. Kumar, S. Prakash, H. Jani, R. Medwal, M. Mishra, R. S. Rawat, T. Venkatesan, N. Wang and R. Singh, *Adv. Funct. Mater.*, 2021, **31**, 2100200.
67 W. Zhu, Y. Fan, C. Li, R. Yang, S. Yan, Q. Fu, F. Zhang, C. Gu and J. Li, *Nanoscale*, 2020, **12**, 8758–8767.
68 Y. Fan, N.-H. Shen, F. Zhang, Q. Zhao, H. Wu, Q. Fu, Z. Wei, H. Li and C. M. Soukoulis, *Adv. Opt. Mater.*, 2019, **7**, 1800537.
69 Z. Wei, X. Liu and Y. Cao, *Front. Phys.*, 2020, **8**, 90.
70 Y. Fan, X. He, F. Zhang, W. Cai, C. Li, Q. Fu, N. V. Sydorchuk and S. L. Prosvirnin, *Research*, 2021, **2021**, 9754083.
71 R. Yang, J. Lou, F. Zhang, W. Zhu, J. Xu, T. Cai, Q. Fu, H. Li and Y. Fan, *Adv. Photonics Res.*, 2021, **2**, 2100103.
72 C. Huang, J. Liao, C. Ji, J. Peng, L. Yuan and X. Luo, *Adv. Opt. Mater.*, 2021, **9**, 2001950.
73 C. Huang, C. Zhang, J. Yang, B. Sun, B. Zhao and X. Luo, *Adv. Opt. Mater.*, 2017, **5**, 1700485.
74 H. Kwon and A. Faraon, *ACS Photonics*, 2021, **8**, 2980.
75 Y. Yang, H. Kim, T. Badloe and J. Rho, *Nanophotonics*, 2022, **11**, 4123–4133.
76 K. Tanaka, D. Arslan, S. Fasold, M. Steinert, J. Sautter, M. Falkner, T. Pertsch, M. Decker and I. Staude, *ACS Nano*, 2020, **14**, 15926.
77 D. Wang, Y. Hwang, Y. Dai, G. Si, S. Wei, D. Y. Choi, D. E. Gomez, A. Mitchell, J. Lin and X. Yuan, *Small*, 2019, **15**, e1900483.
78 R. Zhang, Q. Zhao, X. Wang, K. M. Lau, T. K. Yung, J. Li and W. Y. Tam, *Nanophotonics*, 2022, **11**, 495.
79 H. Cheng, Z. Liu, S. Chen and J. Tian, *Adv. Mater.*, 2015, **27**, 5410–5421.
80 Z. Wei, H. Li, W. Xu and Y. Cao, *Front. Phys.*, 2021, **8**, 632902.
81 C. Menzel, C. Rockstuhl and F. Lederer, *Phys. Rev. A: At., Mol., Opt. Phys.*, 2010, **82**, 053811.
82 C. Menzel, C. Helgert, C. Rockstuhl, E. B. Kley, A. Tunnermann, T. Pertsch and F. Lederer, *Phys. Rev. Lett.*, 2010, **104**, 253902.